



Published in final edited form as:

Nanoscale. 2009 October 21; 1(1): 138–152. doi:10.1039/b9nr00053d.

Random Walk of Single Gold Nanoparticles in Zebrafish Embryos Leading to Stochastic Toxic Effects on Embryonic Developments

Lauren M. Browning[†], Kerry J. Lee[†], Tao Huang, Prakash D. Nallathamby, Jill E. Lowman, and Xiao-Hong Nancy Xu^{*}

Department of Chemistry and Biochemistry, Old Dominion University, Norfolk, Virginia 23529

Abstract

We have synthesized and characterized stable (non-aggregation, non-photobleaching and non-blinking), nearly monodisperse and highly-purified Au nanoparticles, and used them to probe transport of cleavage-stage zebrafish embryos and to study their effects on embryonic development in real time. We found that single Au nanoparticles (11.6 ± 0.9 nm in diameter) passively diffused into chorionic space of the embryos via their chorionic-pore-canals and continued their random-walk through chorionic space and into inner mass of embryos. Diffusion coefficients of single nanoparticles vary dramatically (2.8×10^{-11} to 1.3×10^{-8} cm²/s) as nanoparticles diffuse through various parts of embryos, suggesting highly diverse transport barriers and viscosity gradients of embryos. The amount of Au nanoparticles accumulated in embryos increase with its concentration. Interestingly, their effects on embryonic development are not proportionally related to the concentration. Majority of embryos (74% on average) incubated chronically with 0.025-1.2 nM Au nanoparticles for 120 h developed to normal zebrafish, with some (24%) being dead and few (2%) deformed. We developed a new approach to image and characterize individual Au nanoparticles embedded in tissues using histology sample preparation methods and LSRP spectra of single nanoparticles. We found that Au nanoparticles in various parts of normally developed and deformed zebrafish, suggesting that random-walk of nanoparticles in embryos during their development might have led to stochastic effects on embryonic development. These results show that Au nanoparticles are much more biocompatible (less toxic) to the embryos than Ag nanoparticles that we reported previously, suggesting that they are better suited as biocompatible probes for imaging embryos *in vivo*. The results provide powerful evidences that biocompatibility and toxicity of nanoparticles highly depend on their chemical properties, and the embryos can serve as effective *in-vivo* assays to screen their biocompatibility.

Keywords

biocompatibility; diffusion and transport; embryos; gold nanoparticle; *In vivo* imaging; single nanoparticle optics; toxicity; zebrafish

Introduction

Gold (Au) nanoparticles have been used for a variety of applications over 400 years.^{1, 2} Because Au possesses inert chemical properties, it has been widely considered as one of

^{*} To whom correspondence should be addressed: xhxu@odu.edu; www.odu.edu/sci/xu/xu.htm; Tel/fax: (757) 683-5698.

[†] These authors contributed equally to this work.

most stable and biocompatible materials. Therefore, Au nanoparticles have been suggested as potential biocompatible probes for living cellular imaging and as target-specific vehicles for drug delivery.³⁻⁸ However, studies of biocompatibility and toxicity of Au nanoparticles in various types of cells yield inconclusive results: some studies show toxic effect and high-dependence of toxicity on nanoparticle sizes and their surface functional groups, while other studies exhibit no significant cytotoxicity.⁶⁻¹⁴ Many studies did not use purified Au nanoparticles, or examine any other chemicals present in Au nanoparticle solutions, or well characterize physical properties (e.g., possible size change and aggregation) of Au nanoparticles in buffer solution and cell culture media during the experiments, leading to inconclusive results.⁶⁻¹⁴ Furthermore, study of biocompatibility and toxicity of Au nanoparticles in living animals is still not yet fully explored.^{14, 15}

As noble metal nanoparticles, Au nanoparticles show unique optical properties such as localized surface plasmon resonance (LSPR), which is highly dependent upon their size, shape and surrounding environments.¹⁶⁻²³ Single Au nanoparticles exhibit strong Rayleigh scattering, allowing them to be directly observed and characterized using dark-field optical microscopy and spectroscopy (DFOMS) in real time.^{4, 24-26} Their size-dependent LSPR spectra of single nanoparticles allow us to characterize the sizes of individual nanoparticles *in vivo* (in living animals) in real time using DFOMS, showing a great promise for imaging *in vivo*.^{24, 26-31} Nonetheless, it is essential to determine their potential toxicological effects *in vivo*, prior to fully using them in living organisms.

Unfortunately, current nanotoxicity studies are carried out using a wide variety of cell lines and different types of living organisms, leading to impossible comparison of results among different studies, and inconclusive and conflict reports.^{7, 12-15} Conventional cytotoxicity assays are typically designed for ensemble measurements, which is inadequate to assess toxicity of nanoparticles at single-cell level, because nanoparticles quite often are unevenly distributed among individual cells, which demands the study of nanotoxicity at the single-cell resolution. More importantly, nanoparticles are very different from conventional chemicals and drugs, which requires special cares to prevent them from aggregation *in situ*, and needs new tools to characterize individual nanoparticles *in situ* in real-time. Regrettably, many current nanotoxicity studies did not take required cares to prevent aggregation of nanoparticles during the experimental duration, and did not develop new tools to characterize stability (non aggregation) and sizes of nanoparticles *in situ* in real-time.^{7, 12-14, 32, 33}

It is well known that physical and chemical properties of nanoparticles highly depend upon their sizes, shapes, surface properties (e.g., surface functional group and charges), embedded solvents, and the way that they were prepared and purified.¹⁶⁻²³ Their chemical and physical properties will surely affect their interactions with living organisms, and define their biocompatibility and toxicity in given living organisms. Therefore, it will be misleading if one tries to compare the study of one type of nanoparticles in one living organism with other types of nanoparticles in other living organisms.

To overcome the limitations of current nanotoxicity studies, we have developed: (i) new methods to prepare stable (non-aggregated) and purified model nanoparticles (e.g., different sizes and surface functional groups of Au and Ag nanoparticles); (ii) real-time imaging tools (e.g., DFOMS) for characterizing sizes of individual nanoparticles *in vivo* in real-time; and (iii) effective *in vivo* assays (zebrafish embryos) for screening and probing biocompatibility and toxicity of our model nanoparticles,^{24-29, 31} aiming to depict the dependence of biocompatibility and toxicity of nanoparticles on their physical and chemical properties, and their underlying mechanisms.

In our previous study, we used early development (cleavage-stage) of zebrafish embryos to study the transport, dose-dependent biocompatibility and toxicity of purified silver (Ag) nanoparticles (11.6 ± 3.5 nm in diameter).²⁸ In this study, we select the same cleavage-stage of zebrafish embryos as an *in vivo* model system to study the transport mechanism and dose-dependent biocompatibility of the same size of purified Au nanoparticles, aiming to investigate the dependence of biocompatibility and toxicity of nanoparticles on their chemical properties. Study of the transport and effects of nanoparticles on embryonic development can also provide new insights into how nanoparticles affect embryonic development and offer new opportunities to develop biocompatible nanoparticle tools for a variety of applications, including *in vivo* imaging and drug delivery.

Zebrafish (*Danio rerio*) have been used extensively as a vertebrate model for embryological development study because of its small size, short breeding cycle, and wealthy genetic data base.³⁵⁻⁴⁰ Zebrafish embryos are transparent throughout every developmental stage and develop outside their mothers, allowing direct observation of the development of all internal organs without disturbing the embryos.⁴⁰⁻⁴² The embryonic development is rapid: the first stages of development are completed in the first 24 hours post-fertilization (hpf); the normal embryo hatches by 72 hpf and fully develops at 120 hpf.⁴⁰⁻⁴² Zebrafish can spawn large numbers of embryos, which can serve as effective and inexpensive *in vivo* assays for screening of biocompatibility and toxicity of nanoparticles. Primary developmental mutations identified in zebrafish have close counterparts in other vertebrates,^{35, 37, 40} suggesting that zebrafish can be used effectively as a model for better understanding the developmental processes of higher organisms, including humans. Furthermore, fish (an important aquatic species) are renowned for their ability to bioconcentrate trace contaminants in the environment. Human consumption of fish will lead to the direct impact of potential releasing of nanoparticles into the environment on human. The unique features of zebrafish allow us to probe transport and diffusion of individual Ag and Au nanoparticles inside the embryos, study their effects on the embryonic development in real time, and use them as effective *in vivo* assays for screening biocompatibility and toxicity of nanoparticles and for possible monitoring of their potential environmental impacts.^{28, 29}

Results and Discussion

Synthesis and Characterization of Au nanoparticles

As described in the Methods, we synthesized Au nanoparticles by reducing HAuCl_4 with sodium citrate.^{2, 34} We carefully washed the Au nanoparticles to remove any chemicals from the synthesis using centrifugation, and prepared highly purified and stable (non-aggregated) Au nanoparticles. We determined concentrations, sizes and optical properties of Au nanoparticles through each washing step as described in Method and Supporting Information. We further characterized the concentrations, sizes, and optical properties of the purified Au nanoparticles dispersed in egg water (1.0 mM NaCl in DI water) for 120 h using UV-vis absorption spectroscopy, dynamic light scattering (DLS), high-resolution transmission electron microscopy (HRTEM), and single-nanoparticle dark-field optical microscopy and spectroscopy (DFOMS) (Figures 1 and 2), aiming to determine their stability in egg water throughout the entire incubation period.

The absorbance spectra of freshly prepared and purified nanoparticles before and after incubating with egg water for the entire experimental duration of 120 h (5 days) show an absorbance peak of 0.35 and a peak wavelength of 520 nm (FWHM = 53 nm) (Figure 1A). This result indicates that the Au nanoparticles are very stable in the egg water and remain non-aggregated over 120 h, suggesting that we can use the nanoparticles to monitor the entire development of zebrafish embryos, which takes 120 h. We further characterized the sizes of the Au nanoparticles using HRTEM before and after incubation with egg water for

120 h, showing that the average sizes of Au nanoparticles remain essentially the same at 11.6 ± 0.9 nm (Figures 1B and C). We also measured the sizes of Au nanoparticles in egg water over 120 h using DLS, showing that the sizes of Au nanoparticles remain unchanged at 11.9 ± 1.6 nm. The nanoparticles are hydrated in the solution. Thus, their sizes measured by DLS appear to be slightly larger than those determined using HRTEM.

We characterized the optical properties of individual Au nanoparticles using DFOMS. The representative optical image of single Au nanoparticles in Figure 2A shows that the majority of the Au nanoparticles under dark-field microscope are green, with few being orange. A color distribution of single Au nanoparticles in Figure 2B illustrates that $(88 \pm 4)\%$ of nanoparticles are green, with $(12 \pm 4)\%$ being orange. We determined the color distribution of single nanoparticles in egg water over 120 h and found that they remained essentially unchanged over time, further demonstrating that single Au nanoparticles are stable (non-aggregated) in egg water over time.

Representative localized surface plasmon resonance spectra (LSPR spectra) of single Au nanoparticles acquired by DFOMS in Figure 2C show the peak wavelength of 565 nm (green color) (FWHM = 75 nm) and 600 nm (orange color) (FWHM = 59 nm), respectively. Single green Au nanoparticles show lower scattering intensity than the orange nanoparticles, suggesting that green ones are smaller than the orange ones. By comparing the histogram of color distribution of single nanoparticles in Figure 2B with size distribution of single nanoparticles determined by HRTEM, we found that green nanoparticles are correlated with 9-13 nm Au nanoparticles while orange nanoparticles are associated with 13.5-15 nm Au nanoparticles.

As described by Mie theory, optical properties (LSPR spectra) of noble metal nanoparticles (e.g., Au, Ag) depend on their size, shape, surrounding environment, and dielectric constant of the embedding medium.^{18, 19, 23} As their spherical shape, surrounding environment, and dielectric constant of the embedding medium remain essentially in constant, peak wavelength of LSPR spectra of single nanoparticles vary proportionally to the volume of single nanoparticles, and scattering intensity of single spherical nanoparticles are proportional to the sixth power of its radius.^{18, 19} These unique optical properties allow us to use their color-index as size-index or intensity-index as size-index to determine sizes of single Au nanoparticles in solution in real time using DFOMS, as we reported previously for the study of single Ag nanoparticles.^{24-26, 28-30}

We further characterized the photostability of single Au nanoparticles by acquiring sequential optical images of single Au nanoparticles using DFOMS while these nanoparticles were constantly irradiated under a dark-field microscope illuminator (30 W halogen) over 12 h. The nanoparticles were exposed to white-light illumination power of (0.070 ± 0.001) Watt at the sample stage (focal plane of dark field) during the entire experiment. We measured the scattering intensity of individual nanoparticles within a 20×20 pixel area (squared in Figure 2A) and average background intensity of several detection areas with the same size of detection volume (20×20 pixel) in the absence of nanoparticles (dash-squared in Figure 2A). We then subtracted the average background intensity from the integrated intensity of single nanoparticles and individual background areas and plotted the subtracted integrated intensity of individual nanoparticles and background as a function of time (Figure 2D). These plots show that the scattering intensity of single Au nanoparticles remains essentially unchanged over time. The slight fluctuations of scattering intensity of single nanoparticles are similar to those observed from background, suggesting that these fluctuations might be attributable to intensity fluctuation of the microscope illuminator or to dark noise of the CCD camera. Therefore, these results demonstrate that single Au nanoparticles are photostable and do not suffer photodecomposition and blinking, allowing

us to use them as photostable probes to continuously probe the diffusion and transport dynamics throughout the early development of zebrafish embryos and investigate potential effects of single Au nanoparticles on the embryonic developments.

Diffusion and Transport of Single Au Nanoparticles in Cleavage-stage Embryos

To determine whether individual Au nanoparticles can transport into living zebrafish embryos and its transport mechanism (active or passive transport pathways), we incubated the purified Au nanoparticles with the cleavage stages of zebrafish embryos and imaged the diffusion and transport of single nanoparticles into the cleavage-stage embryos and inside the embryos in real-time. The results in Figures 3-4 show that single Au nanoparticles (green and orange nanoparticles as illustrated in Figure 2C) can diffuse into embryos via chorionic pore canals on chorionic layers and into the inner mass of embryos. High-resolution black/white CCD images in Figures 3-4 illustrate intra-embryonic structures in great details, in which single Au nanoparticles exhibit higher scattering intensity (much brighter) than any debris of embryos. We further characterized LSPR spectra (colors) of single Au nanoparticles observed in Figures 3-4 using DFOMS, showing the spectra of individual nanoparticles are similar to those in Figure 2C. The unique LSPR spectra of single Au nanoparticles allow us to distinguish them from any possible tissue debris or vesicle-like particles in embryos, because unlike Au nanoparticles, tissue debris do not possess plasmonic resonance and do not exhibit LSPR spectra (colors).

An optical image of cleavage-stage embryo in Figure 3A shows chorion, chorionic space (CS), yolk sac (YS), and inner mass of embryo (IME). We focus on probing the transport of single Au nanoparticles at the interface of the chorion with egg water (chorionic layers) and at the interface of inner mass of embryo with chorionic space as squared by (B-C) in Figure 3A, respectively. Sequential dark-field optical images of chorionic layers (the interface of the chorion with egg water) in Figure 3B illustrate the transport of single Au nanoparticles, as circled, from the egg water into the chorionic space via chorionic pore canals. We clearly visualized arrays of well-organized chorionic pore canals (as squared in Figure 3B: a) on chorionic layers and found each pore ranges 0.5 - 0.7 μm in diameter, and is about 1.5 - 2.5 μm apart. This result agrees well with what we reported previously²⁸ and as determined by TEM.⁴³ Sequential dark-field optical images of the interface of chorionic space (CS) with inner mass of embryo (IME) show the transport of single Au nanoparticles, as circled, from the chorionic space into the inner mass of the embryo (Figure 3C). The dashed lines in Figure 3C outline the interface of the chorionic space and the inner mass of embryo.

To further determine their transport mechanisms (active or passive transport pathway), we investigate each diffusion trajectory of single nanoparticles in egg water, entry into chorionic space, in chorionic space, and further into inner mass of the embryo (Figure 4A) using the concept of 2D mean-square-displacement (MSD) and diffusion models [e.g., active (directed) diffusion, simple passive or stationary Brownian diffusion].^{44, 45} According to the diffusion models of single nanoparticles, plots of MSD versus diffusion time interval show distinctive curves for active (directed) diffusion, simple passive Brownian diffusion, and stationary Brownian diffusion, respectively.^{44, 45}

We tracked the diffusion of single nanoparticles in various parts of embryos in real time using real-time square-displacement (RTSD) (diffusion distance), instead of average (mean) of square-displacement, because viscosity gradients and various transport barriers in embryos can vary diffusion coefficient of single nanoparticles in embryos.²⁸ We use this approach to probe the diffusion model and transport pathway of single nanoparticles, and transport barriers and viscosity of the different parts of embryos (e.g., chorionic layer, chorionic space, inner mass of embryo) in real time. We calculate the diffusion coefficient

(D) of single nanoparticles in simple Brownian motion by dividing the slope of a linear plot of square-displacement versus time by 4 (Note: $RTSD = 4D\Delta t$) (Figure 4B).

Representative diffusion trajectories of individual Au nanoparticles with an identical orange color (size) (Figure 4A) show: (a) a single Au nanoparticle is diffusing into the embryo via chorionic pores at the exterior surface of chorionic layer; (b) a single Au nanoparticle is diffusing into the inner mass of embryo from chorionic space; and (c) a single Au nanoparticle is diffusing in chorionic space. Note that we characterized orange color (LSPR spectra) of single Au nanoparticles as shown in Figure 2C-a, allowing us to identify individual Au nanoparticles in embryos.

Plots of RTSD of these single Au nanoparticles versus time (Figure 4B: a) illustrate distinctive diffusion patterns of single Au nanoparticles in various parts of the embryo. For instance, we found a restricted diffusion pattern (stationary Brownian diffusion),^{28, 44, 45} as the single Au nanoparticle diffused into chorionic space of the embryo from egg water via chorionic pores (Figure 4B: a-i), suggesting that single Au nanoparticle navigated through the pores and was tangled and trapped in the pores from time to time. The duration of single Au nanoparticles passing through the pores in chorionic layers ranges from 0.8 to 10 s. The diffusion coefficients of single nanoparticles vary as it diffuses from egg water to the chorionic layers, passing through the chorionic pores, and into chorionic space, ranging from 2.9×10^{-11} to 1.0×10^{-8} cm²/s with an average of $(2.3 \pm 1.9) \times 10^{-9}$ cm²/s.

In contrast, the diffusion of a single Au nanoparticle into the inner mass of embryo from chorionic space shows much less degree of restricted diffusion pattern and the nanoparticle diffuses freely in simple random Brownian motion (Figure 4B: a-ii), suggesting that transport from chorionic space into the inner mass of embryos is less restricted than chorionic layers. These results imply that the transport barrier at the chorionic layer (the interface of chorionic space and egg water) is higher than at the interface of the inner mass of embryo and chorionic space, suggesting a much better protected surface (chorionic layer) of chorionic space than the inner mass of embryos. The diffusion coefficients of single nanoparticles vary as it diffuses to and through the interface of chorionic space and inner mass of embryos, ranging from 1.0×10^{-9} to 9.5×10^{-9} cm²/s with an average of $(3.3 \pm 2.4) \times 10^{-9}$ cm²/s. Interestingly, diffusion of single Au nanoparticles in chorionic space exhibits simple random Brownian motion with uneven diffusion coefficients, ranging from 3.9×10^{-10} to 1.3×10^{-8} cm²/s with an average of $(4.9 \pm 0.8) \times 10^{-9}$ cm²/s. This result suggests a highly heterogeneous chorionic space with various viscosities, which is similar to what we reported previously.^{28, 29}

The results show that Au nanoparticles can diffuse into every part of embryos from egg water via passive Brownian diffusion (no active transport mechanism), because the plots of RTSD versus time in Figure 4B show same characteristics as those described in diffusion models^{44, 45} for simple passive Brownian diffusion and stationary Brownian diffusion, but not for directed (active) Brownian diffusion. Thus, individual Au nanoparticles are not transported into embryos from egg water or inside embryos via active transport pathways (e.g., uptake of nanoparticles driven by the energy of living embryos).

We also characterized the diffusion models and diffusion coefficients (D) of single green and orange Au nanoparticles in egg water (Figure 4B: b) to determine the possible variation of diffusion coefficient of individual nanoparticles due to the slight variation of their sizes (radius), which serves as a control experiment to determine the variation of diffusion coefficients among single nanoparticles. We found that single orange and green Au nanoparticles show simple Brownian diffusion in egg water with D of $(1.3 \pm 1.0) \times 10^{-8}$ and $(2.7 \pm 2.5) \times 10^{-8}$ cm²/s, respectively. It is well known that diffusion coefficients of single

nanoparticles are inversely proportional to their radius, as described by the Stoke-Einstein equation, $D = kT/(6\pi\eta a)$, which shows that the diffusion coefficient (D) depends on the viscosity of medium (η) and the radius (a) of solute (nanoparticle).⁴⁶⁻⁴⁸ As we described previously in Figures 1 and 2, the Au nanoparticles with LSPR spectra (colors) at green and orange region are correlated with nanoparticles with 9-13 nm and 13.5-15 nm in diameter, respectively. Thus, the diffusion coefficient of the larger nanoparticles (15 nm) is about twice smaller than that of the smaller nanoparticles (9 nm), as shown in Figure 4B: b. Note that the shapes of nanoparticles are not perfectly spherical. Thus, the aspect ratios of individual nanoparticles vary, which also contribute to the small variation in their diffusion coefficients.

We studied the diffusion coefficients of same color (radius) of Au nanoparticles in embryos and compared them with those in egg water, showing that the various diffusion coefficients observed in three different parts of embryos (Figure 4B: a) are indeed attributable to the viscosity gradient and transport barrier of embryos, but not the different radius of individual nanoparticles. The diffusion coefficients of single Au nanoparticles inside the chorionic space (Figure 4B: a-iii) are about 2-110 times smaller than those nanoparticles with identical orange color (size) in egg water (Figure 4B: b-i), showing a wide variation of the viscosity gradients in chorionic space.

Imaging and Characterization of Individual Au Nanoparticles in Embryos

We imaged and characterized nanoparticles accumulated and embedded in living embryos using DFOMS as cleavage-stage embryos are incubating with 1.2 nM Au nanoparticles for 4 h, during which the embryos developed from the cleavage stage to gastrulation stage (Figure 5). We observed green and orange Au nanoparticles in various parts of the embryos, as those circled in Figure 5A, which shows that single Au nanoparticles are embedded in the pores of chorionic layers (on the chorionic surface) (Figure 5A: b-c), inside chorionic space (Figure 5A: d) and inner mass of the embryo (on the surface of embryonic cells in Figure 5A: e). We found LSPR spectra of these embedded single nanoparticles are similar to those observed in Figure 2C, showing that embedded color nanoparticles are indeed Au nanoparticles. Notably, the cleavage-stage and gastrulation-stage embryos have not yet developed any pigmentation, and any cellular and tissue debris of embryos appear white under dark-field microscope and do not show signature LSPR spectra (colors) of single Au nanoparticles. Thus, the unique feature of LSPR spectra of single Au nanoparticles allows us to distinguish them from any possible tissue debris or vesicle-like particles in embryos.

We found that majority of nanoparticles diffused into the chorionic space and some of them were overlapped with chorionic pore canals (Figure 5A: b-c). The representative LSPR spectra (colors) of individual nanoparticles in chorionic space (Figure 5A: b) show the similar peak wavelength as those observed in egg water in Figure 2C. This result indicates that majority of nanoparticles remain non-aggregated inside embryos. Otherwise, we would have observed a significant red shift of LSPR spectra of individual nanoparticles. Note that images in Figure 5A were acquired in a whole living embryo in real time. Thus, the entire embryos were filled with nanoparticles, leading to high background in color images (Figure 5A:b-e).

We also incubated cleavage-stage embryos with various concentrations of Au nanoparticles, and imaged Au nanoparticles accumulated in embryos, aiming to determine the concentration-dependence of accumulated Au nanoparticles in embryos. The color images in Figure 5B clearly show that the colors of embryos (6 hpf) depend on the incubation concentration of Au nanoparticles, showing colorless embryos in egg water (the absence of Au nanoparticles), the light reddish and darken burgundy (color of Au nanoparticles in solution) as cleavage-stage embryos are incubated with 0, 0.05, 0.20, and 1.20 nM Au

nanoparticles for only 4 h. This result indicates that the amount of Au nanoparticles accumulated in embryos increases as Au nanoparticle concentration increases, suggesting that concentration-gradient of Au nanoparticles may be the driven force for passive diffusion of Au nanoparticles into the embryos, which agrees well with entry of single nanoparticles into embryos via passive random Brownian motion as shown in Figures 3-4. We are further developing ultrasensitive tools for quantifying total amount of Au nanoparticles in individual living embryos with both temporal and spatial resolution in real-time.

Effects of Au Nanoparticles on Embryonic Development

To probe the possible concentration-dependence of the effects of Au nanoparticles on embryonic development, we incubated cleavage-stage embryos with a series of washed (purified) Au nanoparticle solutions (0, 0.025, 0.05, 0.10, 0.20, 0.40, 0.60, 0.80, 1.0, 1.2 nM) chronically for 120 h, as they fully developed to zebrafish. We imaged the embryos throughout their developmental stages and characterized live, dead and deformed zebrafish as they fully developed at 120 h. Plots of percentages of live, dead and deformed zebrafish versus concentration of Au nanoparticles in Figure 6A illustrate that in the absence of nanoparticles (control experiment), (82 ± 10)% of zebrafish are alive and normally developed, while (18 ± 10)% of zebrafish are dead, but no deformed zebrafish is observed.

Note that the molar concentrations of Au nanoparticles (0, 0.025, 0.05, 0.10, 0.20, 0.40, 0.60, 0.80, 1.0, 1.2 nM) are calculated based upon the number of nanoparticles, as we described previously.^{27, 28, 34} These molar concentrations can be converted to weight/volume concentrations (0, 0.26, 0.53, 1.1, 2.1, 4.2, 6.3 $\mu\text{g/mL}$). Although majority of reported nanotoxicity studies used weight or weight/volume concentration of nanoparticles to describe their findings, we have used molar concentrations of nanoparticles throughout our studies,^{25-29, 31, 34} because molar concentration of nanoparticles truly reflects the number of nanoparticles in solution and accurately describes the proportional change of surface area of nanoparticles as their molar concentration changes. On the contrary, the weigh/volume concentration of nanoparticles cannot accurately describe the number and total surface of nanoparticles in solution. For instance, if the weight/volume concentration of nanoparticles is doubled, the number of nanoparticles and their surface area are not doubled. This is another common mistake that has been made in current nanotoxicity study, which in part leads to conflict reports, because it is incorrect to treat each atom of nanoparticles, instead of individual nanoparticles, like a drug (chemical) molecule in conventional toxicity study. We will report in a separate study that it is inaccurate and misleading to use weight or weight/volume concentration of nanoparticles to describe their concentration-dependent biocompatibility and toxicity.

As Au nanoparticle concentration increases from 0.025 to 1.2 nM, the percentages of alive and normally developed zebrafish decrease slightly within the margin of errors, ranging from (81 ± 13)% to (63 ± 20)%, and the percentages of dead zebrafish increase from (17 ± 11)% to (31 ± 18)%. Interestingly, the percentage of deformed zebrafish ranges from 0 to (6.6 ± 5.5)% in the presence of Au nanoparticles, showing stochastic dependence of nanoparticle concentration.

To ensure that the deformed zebrafish is not caused by any possible residual chemicals from synthesis of nanoparticles, we performed negative control experiments by replacing Au nanoparticles with equal amount of supernatants which was generated from washing nanoparticles. The result in Figure 6B illustrates that the percentages of normally developed live zebrafish and dead zebrafish are essentially same as those observed in the absence of Au nanoparticles in Figure 6A, and deformed zebrafish was not observed in 0, 0.1, 0.60, and 1.2 nM supernatants. Notably, deformed zebrafish were observed only in the embryos treated by

Au nanoparticles, but not in any control experiments (e.g., egg water or supernatants), indicating the toxicity of Au nanoparticles.

We compare normally developed zebrafish (Figure 7A) with abnormally developed zebrafish (Figure 7B) to identify the types of deformities. We found a wide variety of deformities, including finfold (FF) abnormality, tail and spinal cord flexure and truncation (TF), cardiac malformation (CM), yolk sac edema (YSE), and acephaly (headless) and no tail (NT/A), as illustrated in Figure 7B. For instance, in normally developed zebrafish,⁴⁰⁻⁴² the median finfold is a clear, thin membrane around the entire trunk region containing unsegmented fin rays, and the notochord and spinal cord develop straight to the posterior-most tip of the tail (Figure 7A: a and b). In contrast, the tissue structure of the finfold of zebrafish is disorganized and the shapes of the finfold and fin rays are altered (Figure 7B: a-b), which is classified as finfold abnormality. The finfold abnormality is often accompanied by tail and spinal cord flexure and truncation (Figure 7B: a-d). A few embryos exposed to Au nanoparticles also display a form of cardiac malformation in fully developed zebrafish, showing that the pericardial sac region is extremely large and the cardiac ventricle is shrunk (Figure 7B: e-f). The yolk sac region is a bulbous area containing yolk that provides nutrients to the developing embryo, and it shrinks during the later developmental stages in normally developed zebrafish (Figure 7A: c). On the contrary, the yolk sac region of zebrafish (Figure 7B: e-f) is swollen and enlarged, which is called as yolk sac edema.

The severest and rare deformation of zebrafish that we have observed in this study is acephaly (absence of a developed head) and tailless (lacking a distinct tail region) (Figure 7B: g), while the heart of such a deformed zebrafish is still beating. This severely deformed zebrafish shows a small amount of head-like tissue where the head would normally develop, and the tissue was not a fully developed head but rather an irregular formed mass of tissue. Notably, we found only one out of more than thousands of embryos treated with Au nanoparticles developed such acephaly deformation. The comprehensive list of representative deformities of zebrafish is summarized in Table 1S in supporting information. Typically, multiple types of deformations are observed in the same zebrafish (Figure 7B and Table 1S in supporting information), suggesting that some of these deformations may be inter-related.

To illustrate the possible dependence of the number of deformed zebrafish and their deformities (e.g., finfold abnormality, tail and spinal cord flexure and truncation, cardiac malformation, yolk sac edema, acephaly and no tail) on nanoparticle concentration, we plot the number of given types of deformed zebrafish versus nanoparticle concentration (Figure 7C), showing the highest number of deformed zebrafish and most types of deformities at 0.2 nM. To determine possible dependence of a specific type of deformities on nanoparticle concentration, we plot the percentages of given types of deformed zebrafish (= number of one given type of deformed zebrafish divided by the total number of deformed zebrafish at a given concentration) versus nanoparticle concentration (Figure 7D). We found that the percentages of any given type of deformed zebrafish vary with nanoparticle concentration.

Note that we carried out the study of effects of Au nanoparticles on embryonic development of large amount of embryos (60-64 embryos for each experiment) at the single-embryo level (Figures 6-7), aiming to overcome ensemble average measurements and to determine rare events of interest for further investigation. Rare events of interest (e.g., deformities of zebrafish) in Figure 7 would otherwise be buried under ensemble measurements, emphasizing the importance of study of bulk amount of embryos at the single-embryo level. All rare events presented in this study are within the confident level of 95% (or $P=0.05$) for at least four trails of measurements at each nanoparticle concentration (each with 15-20 embryos) analyzed using conventional statistical methods (e.g., t test or Q test). We present

significant difference of observations among each concentration in Methods. Nonetheless, it is important to point out that conventional statistic analysis methods (e.g., t-test) is only suited for analysis of ensemble measurements, but not well suited for analysis of measurements at single-entity level (e.g., single embryo, single cells or single molecule detection).

Taken together, the result in Figure 6 illustrates that cleavage-stage embryos chronically treated with Au nanoparticles for 120 h show small amount of dead and abnormally developed zebrafish. The treated embryos show no clear trend of increase in death or development of deformed zebrafish (types of deformity and severity), as nanoparticle concentration increases. By comparing this result with our previous observations of the effects of the same size and concentration of Ag nanoparticles on the same-stage of embryos,²⁸ we found that Au nanoparticles caused negligible amount of dead and deformed in comparison with Ag nanoparticles, suggesting that Au nanoparticles are much more biocompatible and less toxic to embryos. Nonetheless, the same types of deformed zebrafish were observed in both studies (treating embryos with either Au or Ag nanoparticles). Plausible explanation for these interesting observations is that the random Brownian diffusion of Au nanoparticles inside embryos during their development (120 h) might have led to the accumulation of various amounts of Au nanoparticles in various parts of embryos stochastically.

Imaging and Characterization of Individual Au Nanoparticles in Fully Developed Zebrafish

We imaged and characterized Au nanoparticles embedded in fully developed zebrafish that had been chronically incubated with a given concentration (1.20 nM) of nanoparticles for 120 h since their cleavage stage. We rinsed the zebrafish with DI water to remove external nanoparticles, and fixed it using a histology protocol of tissue sample preparation, as described in Methods.⁴⁹ We prepared ultrathin-layer sections (~0.25–4 μm thickness) of the zebrafish by carefully sectioning the tissues of interest (e.g., eye retina, brain, nasal epithelium, otic capsule, stomach, notochord, swim bladder, and pectoral fin) using a microtome. Finally, we imaged and characterized LSPR spectra of individual nanoparticles embedded in the tissues of interest using DFOMS (Figure 8).

We observed green and orange Au nanoparticles in various parts of the normally developed zebrafish. The results in Figure 8B show that Au nanoparticles are embedded in (i) retina, (ii) brain tissue, (iii) nasal sensory epithelium, (iv) otic capsule, (v) stomach, (vi) notochord, (vii) swim bladder, and (viii) pectoral fin. To enhance the clarity of presentation, we did not circle all embedded nanoparticles in the tissues, but highlighted a few representative nanoparticles embedded in the tissues of interest, as those circled in Figure 8B. LSPR spectra of individual embedded nanoparticles are similar to those observed in Figure 2C, showing that they are indeed Au nanoparticles and majority of embedded nanoparticles remain non-aggregated. If Au nanoparticles were aggregated, the sizes of single nanoparticles would become larger, which would lead to the large shift of peak-wavelength of LSPR spectra of single nanoparticles and color changes of single nanoparticles. We found that the entire section of tissue was fully embedded with nanoparticles. LSPR scattering of individual nanoparticles lighted up their surrounding tissue, creating high background, which was not observed in the tissues of zebrafish untreated with nanoparticles. The unique feature of LSPR spectra of single Au nanoparticles (Figure 2C) allows us to distinguish them from any possible tissue debris, because tissue debris does not exhibit such LSPR spectra (colors) under dark-field microscope.

In comparing with TEM, we found several unique advantages of using histology protocols to prepare tissue samples and using LSPR spectra to characterize embedded individual Au nanoparticles in tissue samples. For example, we can align the zebrafish in a desired position

and perform ultrathin-layer section of specific area of zebrafish. We can characterize the tissue of interest with no need of using staining reagents. Note that staining reagents quite often create significant background and interfere with the identification of individual nanoparticles. We can characterize massive amount of tissue samples rapidly using DFOMS, allowing to carry out extensive studies, generate massive amount of data for statistic analysis, as well as to investigate rare events of interest. We can qualitatively characterize individual Au nanoparticles and determine their sizes using their unique LSPR spectra. Note that LSPR spectra (colors) depend upon size, shape and surrounding environments of nanoparticles. By carefully calibrating LSPR spectra of individual nanoparticles versus their sizes, as described above in Figures 1-2, we can determine sizes of individual nanoparticles at nanometer scale using their LSPR spectra via DFOMS.

Although TEM has been widely used to characterize nanoparticles embedded in cells and tissues, and TEM can offer much higher spatial resolution,^{7, 14, 25, 33} the protocols for TEM sample preparation are cumbersome, and it is nearly impossible to control the alignment of biological organisms (e.g., zebrafish and cells) in resin blocks. Thus, the sections of tissues and cells are generated with random locations of organisms, and it is hard to prepare reproducible sections of interest for comparison, to generate and characterize massive tissue sections for statistic analysis, and to probe rare events of interest. More problematically, to observe the characteristic locations (morphologies) of tissues and cells using TEM, one will need to stain tissues and cells using staining reagents (e.g., uranyl acetate and lead citrate), which quite often creates significant background and interferes identification of nanoparticles embedded in tissues. To undoubtedly identify embedded nanoparticles of interest, one needs to perform EDS of the embedded nanoparticles in tissues and cells. Unfortunately, for sizes of nanoparticles that are smaller than 15 nm, it is extremely challenging to obtain sufficiently high signal of individual nanoparticles over background and noise of surrounding tissues and those reagents used to prepare and fix the tissues and cells. To gain sufficient high EDS signal of individual nanoparticles and reduce noise and background, one can increase voltages of electron beams and/or focus electron beams on the nanoparticles of interest (reduce the size of focus beam to decrease the signal of surrounding tissues). However, current technologies provide micrometer square area of EDS acquisition scanning area. Furthermore, tightening beam area and using higher voltages of electron beam lead to exposure of biological samples to higher energy, resulting in evaporation of surrounding tissues and cells (burn a hole through tissue samples) and loss of signals of interest. These limitations may be the reasons why EDS characterization of embedded nanoparticles (especially smaller nanoparticles, < 15 nm) in tissues and cells have rarely been reported, even though TEM images have been widely displayed in literature.

Therefore, it is crucial to explore new and effective methods to quantitatively and qualitatively image and characterize embedded individual nanoparticles in tissues and cells. We found that the methods that we have reported in this study are more powerful, informative, convenient, and much lower cost than current conventional TEM methods for imaging and characterization of individual nanoparticles embedded in tissues.

By comparing the results in Figure 8 with those in Figure 5, we found that nanoparticles diffused into the early developing embryos stayed inside the embryos during the entire development, which led to the nanoparticles embedded in various parts of fully developed zebrafish. The most intriguing question here is what factor defines the developmental fate of the cleavage-stage embryos to become normally developed, deformed (types of deformation), or dead zebrafish.

As we found in Figure 8, normally developed zebrafish are embedded with significant amount of Au nanoparticles all over their body, and the results in Figures 6 and 7 illustrate

that percentages of dead and deformed zebrafish and types of zebrafish deformation are not proportionally correlated with the concentration of Au nanoparticles. These interesting findings further suggest what we speculated previously that the random walk (random Brownian diffusion) of Au nanoparticles inside embryos during their development (120 h) might have led to stochastic toxic effects on embryonic development. It is quite possible that various parts of embryos might have different responses to Au nanoparticles. If majority portions of embryos are tolerant with Au nanoparticles, it will be entirely stochastic and less concentration-dependent for individual Au nanoparticles to randomly walk into the vital portion of embryos that is much more sensitive to Au nanoparticles, leading to abnormal development of zebrafish. The other possible explanation is that some embryos may be more tolerant with Au nanoparticles than others. Thus, some embryos develop normally, while others are dead or deformed.

Experimental Materials and Methods

Synthesis and Characterization of Gold Nanoparticles

We synthesized gold nanoparticles by reducing 1 mM aqueous solution of $\text{HAuCl}_4 \cdot 3\text{H}_2\text{O}$ with 38.8 mM sodium citrate solution.^{2, 34} As we were refluxing, stirring and boiling the solution for 30 min, we found that the solution color changed from yellow to clear, then to dark purple and finally to burgundy. We stopped heating the solution, continued stirring for 30 min, and filtered the solution using a 0.22 μm filter. The nanoparticles were then washed twice with nanopure water using centrifugation (7735 relative centrifugal force (rcf), Beckman J-21) to remove the byproducts of the reaction and any excess of chemicals in solution. The washed nanoparticles in the pellets were then resuspended in nanopure water and used to incubate with embryos. The supernatant of the nanoparticle solution removed from the last washing step was collected and used as a negative control experiment to monitor the effects of possible trace chemicals involved in nanoparticle synthesis that might be present in the nanoparticle solution. All chemicals were purchased from Sigma and used without further purification or treatment, and the deionized (DI) water (Nanopore, 18 M Ω) was used to prepare solutions and rinse glassware. We characterized the concentrations, optical properties, and sizes of nanoparticles using UV-vis spectroscopy (Hitachi U-2010), dark-field optical microscopy and spectroscopy (DFOMS), high resolution transmission electron microscopy (HRTEM, FEI Tecnai G2 F30 S-Twin), and dynamic light scattering (DLS, Nicomp 380ZLS).

We have well described, in our previous studies, about the design and construction of our dark-field optical microscopy and spectroscopy (DFOMS) (also called as SNOMS) for real-time imaging and characterization of LSPR spectra of single nanoparticles in solution, in single living cells, in zebrafish embryos, and for single molecule detection.^{4, 5, 24-31, 47, 50, 51} In this study, a CoolSnap HQ2 CCD camera and EMCCD camera (PhotonMAX) coupled with a SpectraPro-2150 (Roper Scientific), and a color camera were used for imaging and characterization of LSPR spectra of single Au nanoparticles.

Analysis and Characterization of Molar Concentrations of Au Nanoparticle Solutions

We calculated molar concentration of unwashed Au nanoparticles as described previously.³⁴ We then measured UV-vis absorption spectra of a series of unwashed Au nanoparticle solutions (0.48, 0.79, 1.6, 3.2, 7.9, 14.3 nM), determined the baseline-subtracted absorbance as illustrated in Figure 1A, and plotted the subtracted absorbance versus molar concentrations of Au nanoparticle solution (Figure 1S: A in supporting information), which showed a linear calibration curve with a linear regression of 1.0 and slope of $6.3 \times 10^7 \text{ M}^{-1}$. Using Beer-Lambert law ($A = \epsilon bC$), we found that molar absorptivity (extinction

coefficient) of Au nanoparticle solution at the peak wavelength (λ_{max}) of 520 nm is $6.3 \times 10^7 \text{ M}^{-1} \text{ cm}^{-1}$.

The nanoparticles were spun down using centrifugation to remove the by-products of the reaction and any excess of chemicals in solution, as described above. The nanoparticles in the pellets were well resuspended in nanopure water, to produce the first-time washed nanoparticle solution. We measured UV-vis absorption spectrum of the first-time washed Au nanoparticle solution, showing that the peak wavelength (λ_{max}) of spectrum at 520 nm, which is the same as those observed in the unwashed nanoparticles, suggesting that the size of Au nanoparticles remained unchanged during the centrifugation which was confirmed by HRTEM and DLS measurements (Figure 1). Thus, we used extinction coefficient of unwashed Au nanoparticles ($\epsilon_{520 \text{ nm}} = 6.3 \times 10^7 \text{ M}^{-1} \text{ cm}^{-1}$) to calculate the concentration of the washed nanoparticles as 13.8 nM. We further measured the UV-vis absorption spectra of a series of the first-time washed Au nanoparticle solutions (0.77, 1.5, 3.9, 6.9, 10.8, 13.8 nM) and found their peak wavelengths at 520 nm (Figure 1S: B in Supporting Information). The plot of subtracted absorbance versus concentration of the first-time washed nanoparticles show a linear calibration curve with a linear regression of 1.0 and slope of $6.3 \times 10^7 \text{ M}^{-1}$, and thereby molar absorptivity (extinction coefficient, $\epsilon_{520 \text{ nm}}$) of the first-washed Au nanoparticle solution at the peak wavelength (λ_{max}) of 520 nm is $6.3 \times 10^7 \text{ M}^{-1} \text{ cm}^{-1}$.

Using the same approach, we prepared the second-time washed Au nanoparticles and measured UV-vis absorption spectrum of the second-time washed nanoparticle solution, showing that the peak wavelength (λ_{max}) of spectrum at 520 nm, which is the same as those observed in the first-time washed nanoparticles. The result suggests that the size of Au nanoparticles remained unchanged during the centrifugation, which was confirmed by HRTEM and DLS measurements. Thus, we used the extension coefficient of the first-time washed Au nanoparticles ($\epsilon_{520 \text{ nm}} = 6.3 \times 10^7 \text{ M}^{-1} \text{ cm}^{-1}$) to calculate the concentration of the second-time washed nanoparticles as 6.6 nM. We further measured the UV-vis absorption spectra of a series of the second-time washed Au nanoparticle solutions (0.37, 0.73, 1.8, 3.3, 5.1, 6.6 nM) and found their peak wavelengths at 520 nm (Figure 1S: C in Supporting Information). The plot of subtracted absorbance versus concentration of the second-time washed nanoparticles show a linear calibration with a linear regression of 1.0 and slope of $6.3 \times 10^7 \text{ M}^{-1}$. Thus, molar absorptivity (extinction coefficient, $\epsilon_{520 \text{ nm}}$) of the second-washed Au nanoparticle solution at the peak wavelength (λ_{max}) of 520 nm is $6.3 \times 10^7 \text{ M}^{-1} \text{ cm}^{-1}$.

We also used DFOMS to determine trace amount of individual Au nanoparticles in supernatants. If we found any Au nanoparticles were present in the supernatant, we would further remove them from the supernatant using ultra-centrifugation (L90, Beckman), which allowed the supernatant to serve as a control experiment (all other chemicals, except Au nanoparticles, are present in the solution). Note that we would continue washing cycles (third or fourth washing cycles) until we generated the supernatant that did not affect the embryonic development (clean blank control experiments), which indicated that the nanoparticles were well purified and ready to be used to treat the embryos. In this study and our previous studies,^{28, 29} two-time washed supernatants provided clean and successful control experiments. In other words, the twice-washed nanoparticles are sufficiently pure to be used to study their effects on embryonic development.

Characterization of Photostability of Single Au Nanoparticles

We characterized photostability of single Au nanoparticles by acquiring sequential optical images of single Ag nanoparticles using EMCCD camera with exposure time at 200 ms and interval time of 40.6 ms for the first 5 min and 300 s afterwards while these nanoparticles

were constantly irradiated under dark-field microscope illuminator (30 W halogen) for 12 h. The illumination power at the sample stage (focal plane of dark field) measured using a power meter was (0.070 ± 0.001) watt during the experiment.^{27-29, 31} We calculated the integrated intensity of a 20×20 pixel area where a nanoparticle was presented (as squared in Figure 2A) and the average background intensity of several detection areas with the same size of detection volume (20×20 pixel) in the absence of nanoparticles (as dashed-squared in Figure 2B). By subtracting the average background intensity from the integrated intensity of single nanoparticles and individual background area, we then plotted the subtracted integrated intensity of individual nanoparticles and background as a function of time (Figure 2D). We characterized and identified individual Au nanoparticles using their LSPR spectra (Figure 2C).

Breeding of Zebrafish Embryos

We housed wild type adult zebrafish (Aquatic Ecosystems) in a stand-alone system (Aquatic Habitats), maintained and bred zebrafish as described previously.^{28, 52} Briefly, we placed two pairs of mature zebrafish into a clean 10-gallon breeding tank, and used a light (14 h)-dark (10 h) cycle to trigger breed and fertilization of embryos. We collected the embryos at cleavage stage (8–64-cell stage; 0.75–2.25 hpf), transferred them into a petri dish containing egg water (1.0 mM NaCl in DI water) (NaCl, 99.95%, Sigma), and well rinsed them with egg water to remove the surrounding debris.

Study of Transport and Biocompatibility of Au Nanoparticles in Embryos

To probe the transport of individual Au nanoparticles into embryos in real time, we then placed the cleavage-stage embryos directly into a self-made microchamber, and simultaneously imaged the transport of single nanoparticles into embryos in real time using our DFOMS, while adding purified Au nanoparticle solution into the chamber to prepare desired Au nanoparticle concentrations. The diffusion measurements were completed within minutes.

To determine biocompatibility of Au nanoparticles, we transferred the embryos into 24 well plates (two embryos/well) and incubated them with a series of washed (purified) Au nanoparticle solutions (2.00 mL/well of 0, 0.025, 0.05, 0.10, 0.20, 0.40, 0.60, 0.80, 1.0, 1.2 nM, which is 0, 0.53, 1.1, 2.1, 4.2, 8.4, 12.6 μg per well). The molar concentrations of Au nanoparticles are calculated as we described previously,^{27, 28, 34} and these molar concentrations can also be described as weight/volume concentrations (0, 0.26, 0.53, 1.1, 2.1, 4.2, 6.3 $\mu\text{g}/\text{mL}$). We also incubated embryos with egg water (in the absence of nanoparticles) and the supernatants from washing Au nanoparticles, which were carried out simultaneously as those incubated with Au nanoparticles, serving as control experiments for monitoring untreated embryos and determining possible effects of trace chemicals involved in synthesis of nanoparticles, respectively. We incubated the embryos in the 24-well plates in a water bath at 28.5°C, and observed them at room temperature using an inverted microscope (Zeiss Axiovert 100) at 24, 48, 72, 96, and 120 hpf. We acquired images of the normal, deformed and death of adult zebrafish at 120 hpf using a digital camera and CCD camera. Each experiment was done at least four times and a total of 60 – 64 embryos for each experiment were studied to gain sufficient amount of data for statistic analysis.

Imaging and Characterization of Au Nanoparticles in Embryos and Zebrafish

We imaged and characterized Au nanoparticles accumulated in living embryos using DFOMS as the cleavage-stage embryos were incubated with 1.2 nM Au nanoparticles for 4 h (Figures 3-5).

We also characterized Au nanoparticles embedded in fully developed zebrafish that had been chronically incubated with a given concentration (1.2 nM) of nanoparticles for 120 h since their cleavage stage (Figure 8). The treated zebrafish were rinsed with DI water to remove external nanoparticles, and fixed using a tissue processor (STP 120) and a tissue embedding center (Shandon Histocentre™ 3 Embedding Center) via a histology protocol of tissue sample preparation as described below.

The zebrafish were fixed using chemical fixation (formaldehyde), dehydrated by EtOH, infiltrated with Clear-Rite (isoparaffinic aliphatic hydrocarbons), and finally embedded with paraffin, using a Microm STP-120 Spin Tissue Processor (Thermo Fisher Scientific). The tissue processor contains 12 buckets of solutions and a tissue sample holder that is controlled by computer-programs to automatically move the tissue samples from a solution in one bucket to the other in a desired manner. The solutions in the 12 buckets are arranged in the following order: buckets (i)-(ii): 10% buffered formalin in both buckets for fixation; buckets (iii)-(viii): 50%, 70%, 95%, 100%, 100%, and 100% (v/v) of EtOH/water for dehydration, respectively; buckets (ix)-(x): Clear-Rite in both buckets for removing EtOH from the tissue and infiltrating the tissue with Clear-Rite; buckets (xi)-(xii): paraffin at 60 °C in both buckets for embedding the tissue with paraffin. We placed the zebrafish treated with nanoparticles (or supernatant or untreated, as control experiments) in histo-screen cassettes and transferred the cassettes to the sample holder of the tissue processor, which moved the samples from one bucket to the other, allowing the tissue of zebrafish to be fully immersed in the solution of each bucket for desired duration (20-40 min) to complete histology sample preparation.

For example, the zebrafish were immersed in the first and second bucket containing the 10% buffered formalin for 20 min each, fully infiltrating the tissue of zebrafish with fixative. Note that formaldehyde reacts with the amine groups (NH_2) of tissue proteins and stabilize the tissue in a fixed position, which is widely used as a fixative. Dehydration was then performed to remove water from the tissue of zebrafish by fully immersing the samples into each solution of 50%, 70%, 95%, 100%, 100%, and 100% (v/v) of EtOH/water in buckets (iii)-(viii), for 20 min each. The samples were fully immersed in buckets (ix)-(x) containing Clear-Rite solution, for 20 min each, which allowed Clear-Rite (a solvent miscible with the embedding medium, paraffin) to completely replace EtOH that remained inside the tissue. The samples were finally moved into the last two buckets (xi-xii) containing paraffin at 60 °C and fully immersed in each paraffin solution for 40 min each. The heat (60 °C) causes the Clear-Rite solvent to evaporate, creating spaces in the tissue of zebrafish, which were fully infiltrated with the heated paraffin. Note that it is crucial to completely remove water from the tissue using dehydration process and fully infiltrate the tissue with Clear-Rite in order to appropriately embed the tissue with paraffin and to prevent the formation of the holes in the tissue, which allows us to prepare ultra-thin-layer sections of tissue samples of zebrafish in the following steps.

We then moved the zebrafish with the histo-screen cassettes from the sample holder of tissue processor into a paraffin bath at 60 °C in a Shandon Histocentre 3 embedding center (Thermo Fisher Scientific), and used the embedding center to prepare the tissue sample blocks. The embedding center includes a paraffin bath at 60 °C, a well-controlled nozzle system of the paraffin bath, a hot-plate at 45 °C, and a cold-plate at 0 °C. We filled a thin layer of liquefied paraffin (60 °C) on the bottom of a small histological block mold using the nozzle system of the paraffin bath, removed one zebrafish from the histo-screen cassette to the block mold, and aligned the zebrafish in a desired position in the mold (either vertically or horizontally aligned with the bottom of the mold). The mold was placed on the hot plate (45 °C) to prevent the paraffin from hardening, allowing us to perform the alignment successfully. We then placed the mold on the top of the cold plate (0 °C), which

immediately solidified the paraffin and locked the zebrafish in the desired position inside the paraffin block. We filled up the mold with the paraffin (60 °C), placed the histo-screen cassette on the top of the mold, and left it on the cold plate (0 °C) overnight, allowing the paraffin to solidify completely.

We sectioned the sample block (~ 0.25 - 4 μm thickness) using a Microm HM360 rotary microtome (Thermo Fisher Scientific), and floated each section of the block on a DI water bath (40 °C), allowing the section to well spread over the water surface and create the smoother and thinner section. We then collected the sample using specially designed tissue slides, and dried the slides on a slide warmer (45 °C) overnight. After the slides were dried, we heated the slide in an upright position in an oven at 60 °C for 30 min, allowing the paraffin to slowly melt off the slide to remove the excess paraffin from the tissue.

The sections of the tissue embedded with nanoparticles were directly characterized using our DFOMS (Figure 8). LSPR spectra of individual nanoparticles offer chemical characterization of the nanoparticles (Figure 2C). The methods that we have developed in this study and in our previous studies²⁸ provide a powerful new tool to determine and characterize individual nanoparticles embedded in tissues, and to image the tissues with embedded nanoparticles with no need of staining reagents.

Statistical Analysis

Each experiment related to the study of biocompatibility and toxicity of Au nanoparticles was performed at least four times and a total of 60 – 64 embryos for each experiment were studied to gain sufficient amount of data for statistic analysis, permitting the study of effect of nanoparticles on bulk amount of embryos at the single-embryo level. We present average percentages of normally developed, dead and deformed zebrafish versus concentration of nanoparticles and supernatants (control), from all measurements, with their standard deviations, as shown in Figure 6. We used conventional statistic analysis methods (t-test) to determine the significant difference of the observations of normally developed, deformed and dead zebrafish among different concentrations (0-1.20 nM) of Au nanoparticles in Figure 6A. We found significant difference of normally developed, deformed and dead zebrafish observed at 0.2 nM Au nanoparticle concentration from those observed in the absence of nanoparticles (0 nM, control experiments) with a confident level of 90% (or $P = 0.10$). We observed the significant difference of deformed zebrafish (but not normally developed and dead zebrafish) at 0.2 nM from those in other concentrations (0.40, 0.60, 0.80, 1.0, or 1.20 nM) with a confident level of 90% (or $P = 0.10$), but not significant differences among other concentrations.

We report all unique observations, especially rare deformed zebrafish, in Figure 7C. We have never observed the deformed zebrafish in the absence of Au nanoparticles (control experiments). All rare events presented in this study are within the confident level of 95% (or $P = 0.05$) for four trails of measurements (each with 15-20 embryos) at each nanoparticle concentration, which is analyzed using conventional statistical methods (e.g., t test or Q test). Note that study of embryos at single embryo level allows us to depict the rare event of interest, which otherwise would be buried under ensemble measurements, emphasizing the importance of study of bulk amount of embryos at the single-embryo level.

We investigated over 100 nanoparticles for each measurement of single nanoparticles to gain sufficient data for statistic analysis and for determining their size distribution and color distribution that represents the bulk nanoparticle solution at the single-nanoparticle resolution. We repeat all measurements, including characterization of photostability and LSPR spectra of single nanoparticles, control experiments, and analysis of concentrations of nanoparticle solutions, at least three times, and present representative and average data of all

measurements with standard deviations. All measurements are very reproducible, well beyond the confident level of 95% (or $P = 0.05$). Thus, we do not need to reject any data.

Summary

In summary, we have synthesized and characterized stable (photostable, non-aggregated), nearly monodisperse, and highly-purified Au nanoparticles, and utilized them to study cleavage-stage embryos in real time and to probe their effects on embryonic development. We found that single Au nanoparticles passively diffused into chorionic space of the embryos via their chorionic pore canals and continued their random-walk into inner mass of embryos. Diffusion coefficients of single nanoparticles range from 2.8×10^{-11} to 1.3×10^{-8} cm^2/s , as nanoparticles passively diffuse through various parts of embryos, suggesting highly diverse transport barriers and viscosity gradients of the embryos. A wide range of diffusion coefficients (3.9×10^{-10} to 1.3×10^{-8} cm^2/s) of single nanoparticles in chorionic space suggests its high heterogeneity. We found that the amount of Au nanoparticles accumulated in embryos increase with its concentration. Interestingly, their effects on embryonic development show stochastic dependence on concentration. Majority of embryos (74% on average) incubated chronically with 0.025-1.2 nM Au nanoparticles for 120 h developed to normal zebrafish, with some (24%) being dead and few (2%) deformed. This result is in stark contrast with what we reported previously using Ag nanoparticles,²⁸ showing that Au nanoparticles are much more biocompatible to the embryos than Ag nanoparticles and suggesting that biocompatibility and toxicity of nanoparticles depend on their chemical properties. We describe a new approach to image and characterize individual Au nanoparticles embedded in tissues using histology sample preparation methods and LSRP spectra of single nanoparticles. We found Au nanoparticles in various parts of normally developed zebrafish. Taken together, these interesting findings suggest that the random-walk (Brownian diffusion) of Au nanoparticles in embryos during their development (120 h) causes individual Au nanoparticles walking into different parts of embryos randomly, which might have led to stochastic effects on embryonic development. Work is in progress to further probe what causes the embryos to become normally developed, deformed (various types of deformation) or dead zebrafish, as they are incubated with nanoparticles.

Supplementary Material

Refer to Web version on PubMed Central for supplementary material.

Acknowledgments

This work is supported in part by NSF (NIRT: BES 0507036; DMR 0420304) and NIH (R01 GM076440). Browning, Lee, Nallathamby, and Lowman are grateful for the support of NIH-GRAS (R01 GM076440S1), NSF-GRAS (BES 0541661), Dominion Scholar Fellowship and ODU honor college undergraduate fellowship, respectively. We thank CharFac of University of Minnesota (a NNIN site funded by NSF) for their assistance to characterize Au nanoparticles using HRTEM.

References

1. Daniel MC, Astruc D. Chem Rev 2004;104:293. and references therein. [PubMed: 14719978]
2. Hayat, MA. Colloid Gold: Principles, Methods and Applications. Academic Press; 1989.
3. Schultz S, Smith DR, Mock JJ, Schultz DA. Proc Natl Acad Sci U S A 2000;97:996. [PubMed: 10655473]
4. Xu, XHN.; Patel, RP. Imaging and Assembly of Nanoparticles in Biological Systems. Nalwa, HS., editor. 2005. and references therein

5. Xu, X-HN.; Patel, RP. Nanoparticles For Live Cell Dynamics. Nalwa, HS., editor. 2004. and references therein
6. Chen Y-H, Tsai C, Huang -YP-Y, Chang M-Y, Cheng P-C, Chou C-H, Chen D-H, Wang C-R, Shiau A-L, Wu C-L. *Molecular Pharmaceutics* 2007;4:713. [PubMed: 17708653]
7. Murphy CJ, Gole AM, Stone JW, Sisco PN, Alkilany AM, Goldsmith EC, Baxter SC. *Acc Chem Res* 2008;41:1721. and references therein. [PubMed: 18712884]
8. Perrault SD, Walkey C, Jennings T, Fischer HC, Chan W. *Nano Lett* 2009;9:1909–1915. [PubMed: 19344179]
9. Shukla R, Bansal V, Chaudhary M, Basu A, Bhonde RR, Sastry M. *Langmuir* 2005;21:10644. [PubMed: 16262332]
10. Connor EE, Mwamuka J, Gole A, Murphy CJ, Wyatt MD. *Small* 2005;1:325. [PubMed: 17193451]
11. Khan JA, Pillai B, Das TK, Singh Y, Maiti S. *Chembiochem* 2007;8:1237. [PubMed: 17569092]
12. Pan Y, Neuss S, Leifert A, Fischler M, Wen F, Simon U, Schmid G, Brandau W, Jahnen-Dechent W. *Small* 2007;11:1941. and references therein. [PubMed: 17963284]
13. Brown CL, Whitehouse MW, Tiekink ER, Bushell GR. *Inflammopharmacology* 2008;16:133. and references therein. [PubMed: 18521546]
14. Ray PC, Yu H, Fu PP. *J Environ Sci Health C Environ Carcinog Ecotoxicol* 2009;27:1. and references therein.
15. Fischer HC, Chan WC. *Curr Opin Biotechnol* 2007;18:565. and references therein. [PubMed: 18160274]
16. Kreibig, U.; Vollme, M. *Optical Properties of Metal Clusters*. Springer; 1995.
17. Sun Y, Xia Y. *Analytical Chemistry* 2002;74:5297. [PubMed: 12403584]
18. Bohren, CF.; Huffman, DR. *Absorption and Scattering of Light by Small Particles*. Wiley; 1983.
19. Mie G. *Ann Phys* 1908;25:377.
20. Mulvaney P. *Langmuir* 1996;12:788.
21. Lee KS, El-Sayed MA. *J Phys Chem B* 2006;110:19220. [PubMed: 17004772]
22. Lee PC, Meisel D. *J Phys Chem* 1982;86:3391.
23. Kelly KL, Coronado E, Zhao LL, Schatz GC. *J Phys Chem B* 2003;107:668–677. and references therein.
24. Kyriacou S, Brownlow W, Xu X-HN. *Biochemistry* 2004;43:140. [PubMed: 14705939]
25. Xu X-HN, Brownlow WJ, Kyriacou SV, Wan Q, Viola JJ. *Biochemistry* 2004;43:10400. [PubMed: 15301539]
26. Xu X-HN, Chen J, Jeffers RB, Kyriacou SV. *Nano Letters* 2002;2:175.
27. Huang T, Nallathamby PD, Gillet D, Xu X-HN. *Anal Chem* 2007;79:7708. [PubMed: 17867652]
28. Lee KJ, Nallathamby PD, Browning LM, Osgood CJ, Xu X-HN. *ACS Nano* 2007;1:133. [PubMed: 19122772]
29. Nallathamby PD, Lee KJ, Xu X-HN. *ACS Nano* 2008;2:1371. [PubMed: 19206304]
30. Xu, X-HN.; Song, Y.; Nallathamby, PD. *Probing Membrane Transport Of Single Live Cells Using Single Molecule Detection And Single Nanoparticle Assay*. Xu, X-HN., editor. New Jersey: 2007. and references therein
31. Huang T, Nallathamby PD, Xu X-HN. *J Am Chem Soc* 2008;130:17095. [PubMed: 19053435]
32. Geiser M, Casaulta M, Kupferschmid B, Schulz H, Semmler-Behnke M, Kreyling W. *Am J Respir Cell Mol Biol* 2008;38:371. and references therein. [PubMed: 17947511]
33. Rothen-Rutishauser B, Grass RN, Blank F, Limbach LK, Muhlfeld C, Brandenberger C, Raemy DO, Gehr P, Stark WJ. *Environ Sci Technol* 2009;43:2634. and references therein. [PubMed: 19452928]
34. Xu X-HN, Huang S, Brownlow W, Salatia K, Jeffers R. *J Phys Chem B* 2004;108:15543.
35. den Hertog J. *Biosci Rep* 2005;25:289. [PubMed: 16307377]
36. Hill AJ, Teraoka H, Heideman W, Peterson RE. *Toxicol Sci* 2005;86:6. [PubMed: 15703261]
37. Kahn P. *Science* 1994;264:904. [PubMed: 8178149]

38. Teraoka H, Dong W, Hiraga T. *Congenit Anom (Kyoto)* 2003;43:123. [PubMed: 12893971]
39. Zon LI, Peterson RT. *Nat Rev Drug Discovery* 2005;4:35.
40. Gong, Z.; Korzh, V. *Fish Development and Genetics: The Zebrafish and Medaka Models*. Singapore: 2004. and references therein
41. Kunz, YW. *Developmental Biology of Teleost Fishes*. Springer; 2004.
42. Hoar, WS.; Randall, DJ. *Fish Physiology: The Physiology of Developing Fish, Part A, Eggs and Larvae*. Academic Press; 1988.
43. Rawson DM, Zhang T, Kalicharan D, Jongebloed WL. *Aquaculture Research* 2000;31:325.
44. Kusumi A, Sako Y. *J Cell Biology* 1994;125:1251. and references therein.
45. Kusumi A, Sako Y, Yamamoto M. *Biophys J* 1993;65:2021. [PubMed: 8298032]
46. Tinoco I, Sauer K, Wang J, Puglisi JD. *Molecular Motion and Transport Properties*. 2002
47. Xu X-HN, Jeffers RB, Gao J, Logan B. *Analyst* 2001;126:1285. [PubMed: 11534594]
48. Bard AJ, Faulkner LR. New York. 1980
49. Mohideen M-APK, Beckwith LG, Tsao-Wu GS, Moore JL, Wong ACC, Chinoy MR, Cheng KC. *Developmental Dynamics* 2003;228:414–423. [PubMed: 14579380]
50. Kyriacou SV, Nowak ME, Brownlow WJ, Xu X-HN. *J Biomed Opt* 2002;7:576. [PubMed: 12421124]
51. Xu X-HN, Brownlow WJ, Huang S, Chen J. *Biochem Biophys Res Commun* 2003;305:79. [PubMed: 12732199]
52. Westerfield, M. *The zebrafish book: A Guide for the Laboratory Use of Zebrafish (Danio Rerio *)*. University of Oregon Press Chapters 1-4; 1993. http://zfin.org/zf_info/zfbook/zfbk.html

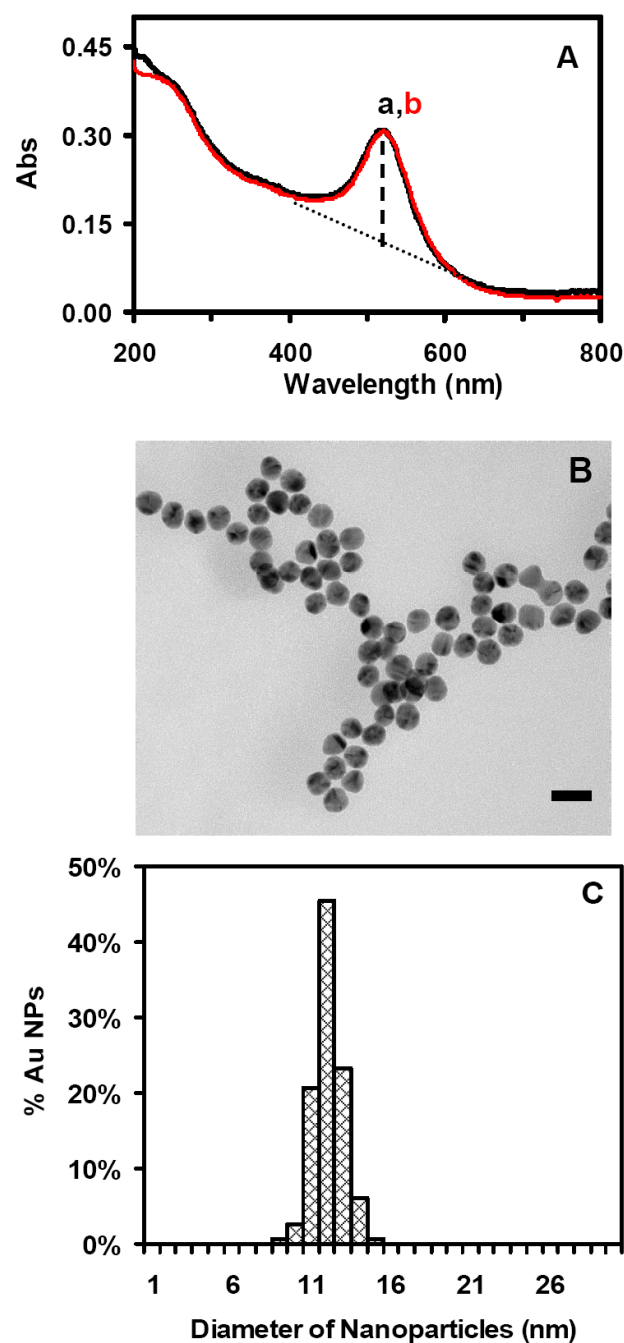


Figure 1.

Characterization of size and stability of Au nanoparticles:

(A) Representative UV-Vis absorption spectra of 1.20 nM Au nanoparticles well-dispersed in egg water at 28 °C for (a) 0 and (b) 120 h show that the spectra with peak absorbance wavelength at 520 nm (FWHM = 53 ± 2 nm) remain unchanged for 120 h. The based-line subtracted absorbance was calculated by subtracting the based-line (dashed-line) from the peak absorbance using a well-known based-line subtraction method. The full width was then determined at the subtracted half-maximum, showing FWHM as 53 ± 2 nm.

(B) Representative HRTEM images of Au nanoparticles show the size and nearly spherical shape of single Au nanoparticles with the average size being 11.6 ± 0.9 nm. Scale bar = 20 nm.

(C) Histogram of size distribution of Au nanoparticles measured by HRTEM show the average size to be 11.6 ± 0.9 nm.

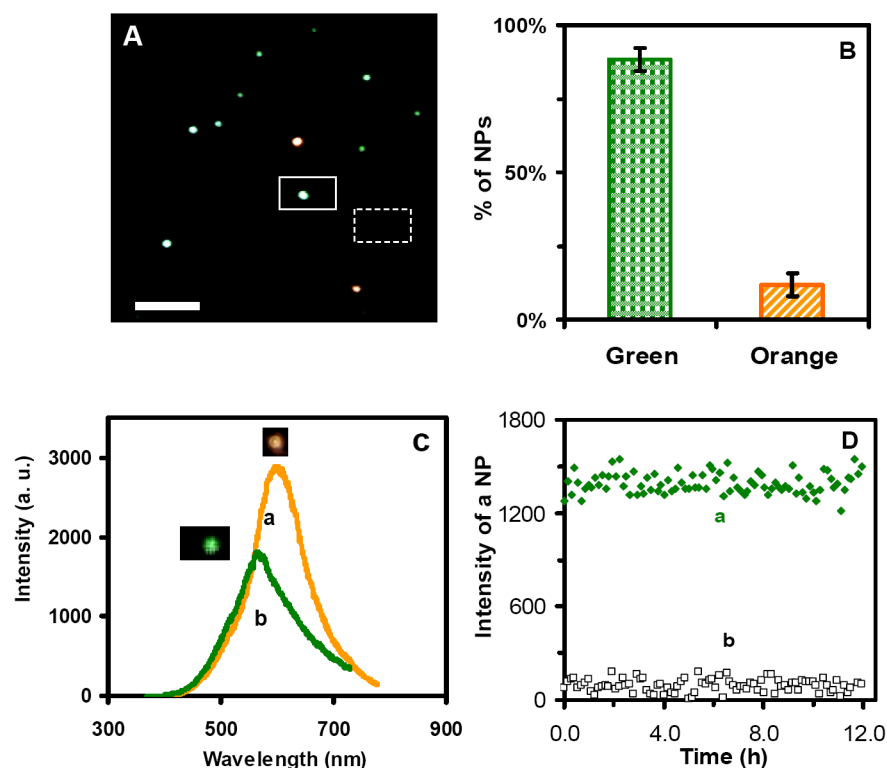


Figure 2.

Characterization of optical properties and photostability of single Au nanoparticles:

(A) Representative dark-field optical image of single Au nanoparticles shows that the majority of nanoparticles are green with some being orange. Scale bar represents 2 μm, which shows the distance among individual nanoparticles, but not the sizes of nanoparticles, because they were imaged under optical diffraction limit.

(B) Histogram of color distribution of individual Au nanoparticles shows that (88 ± 4)% of nanoparticles are green with (12 ± 4)% orange.

(C) Representative LSPR spectra (colors) of single Au nanoparticles show peak wavelengths (λ_{max}) at 565 nm (green) (FWHM = 75 nm) and 600 nm (orange) (FWHM = 59 nm).

(D) Plots of scattering intensity of (a) a representative single green Au nanoparticle and (b) background versus illumination time, show that the intensity of the nanoparticle remains unchanged over time, demonstrating photostability of the nanoparticle.

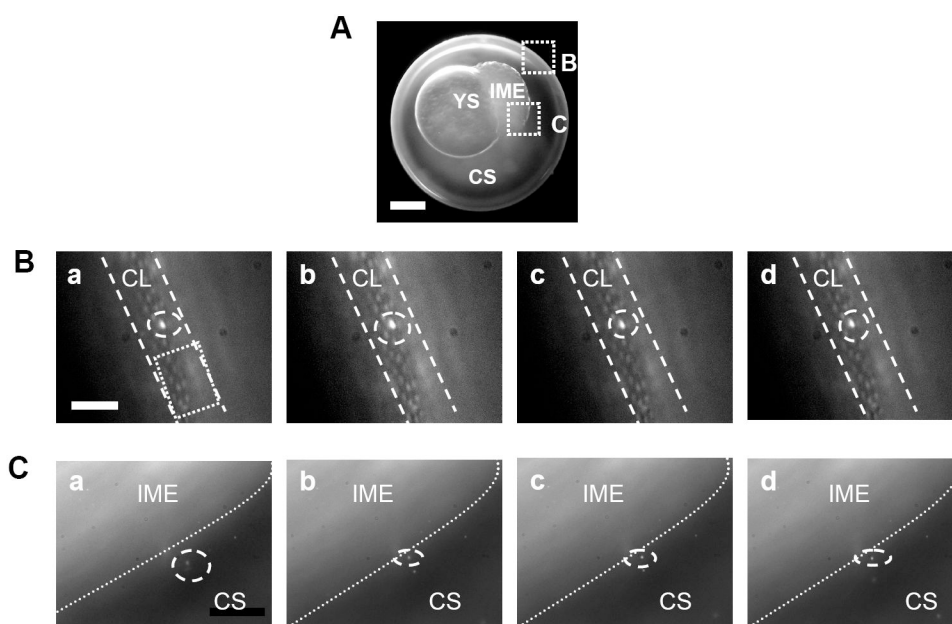


Figure 3. Real-time imaging of diffusion and transport of single Au nanoparticles in a cleavage-stage zebrafish embryo.

(A) Optical image of the cleavage-stage embryo shows chorion, chorionic space (CS), yolk sac (YS), and inner mass of embryo (IME), acquired by CCD camera. The transport of single Au nanoparticles at the interface of the chorion with egg water and at the interface of chorionic space (CS) with inner mass of embryo (IME) is illustrated in (B-C), respectively. Scale bar = 200 μm .

(B) Sequential dark-field optical images on the chorionic layer (CL) illustrate the transport of single Au nanoparticles, as circled, from the egg water into the chorionic space via chorionic pore canals as squared. The array of well-organized chorionic pore canals are clearly visualized and determined as 0.5 - 0.7 μm in diameter and each pore is about 1.5 - 2.5 μm apart. The straight dashed lines outline the chorionic layer (CL). Time interval between: (a) and (b) is 2.75 s; (b) and (c) is 3.92 s; and (c) and (d) is 5.10 s. Scale bar = 10 μm .

(C) Sequential dark-field optical images of the interface of chorionic space (CS) with inner mass of embryo (IME) illustrate the transport of single Au nanoparticles, as circled, from the chorionic space into the inner mass of the embryo. The dashed lines outline the interface of the chorionic space and the inner mass of embryo. Time interval between: (a) and (b) is 5.88 s; (b) and (c) is 5.89 s; and (c) and (d) is 3.14 s. Scale bar = 20 μm . Note that we used LSPR spectra of the nanoparticles, which are similar to those observed in Figure 2C, to identify Au nanoparticles diffusing inside the embryos.

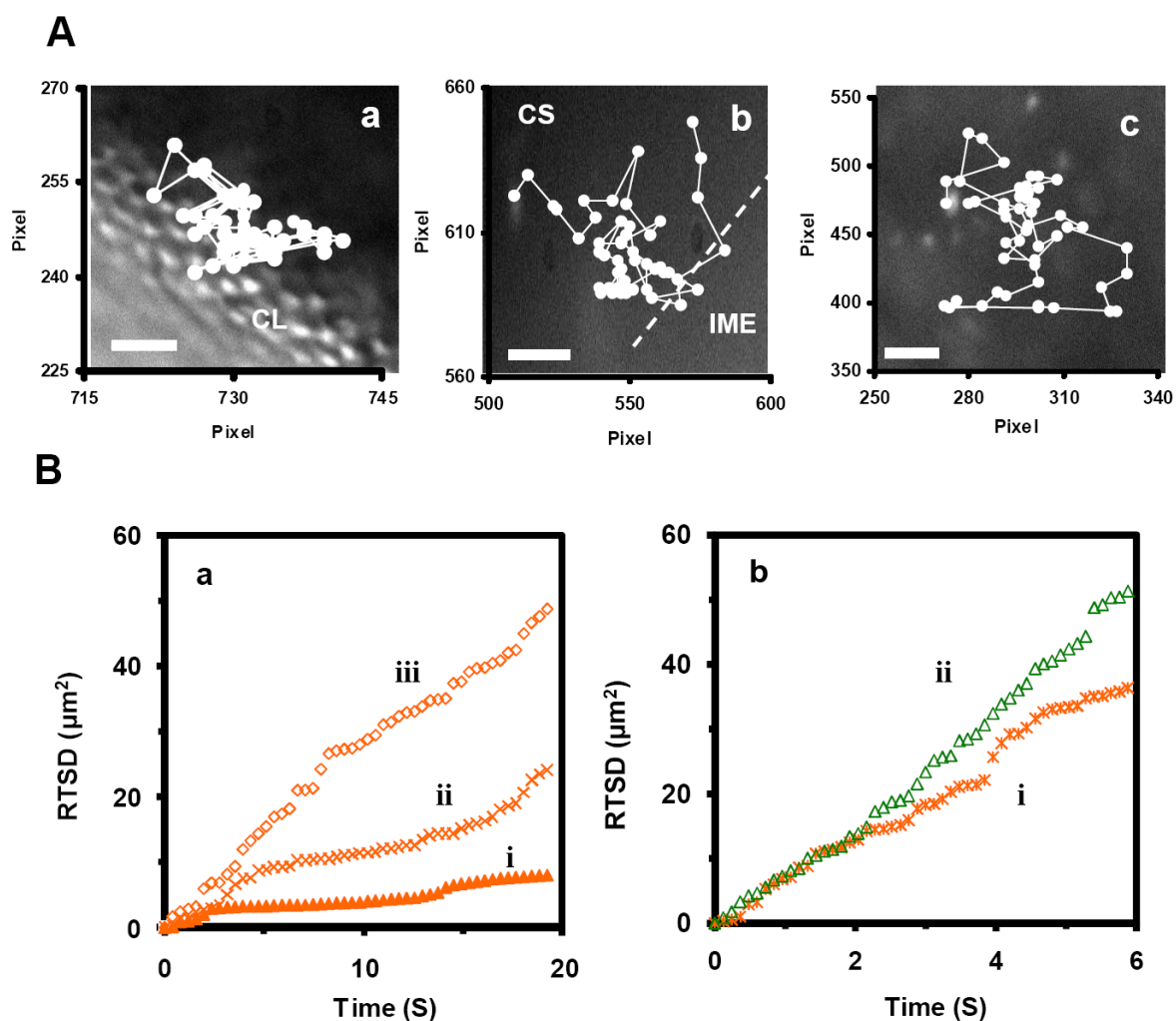


Figure 4.

Characterization of transport and diffusion trajectories of single Au nanoparticles in a cleavage-stage embryo.

(A) Diffusion trajectories of an orange Au nanoparticle at (a) the exterior surface of chorionic layer (CL), (b) at the interface of chorionic space with the inner embryo mass, and (c) in the chorionic space. Scale bar = 5 μm.

(B) Plots of real-time square displacement (RTSD) of single Au nanoparticles as a function of time:

(a) from the diffusion trajectories (a-c) shown in (A), illustrating that the orange Au nanoparticles show (i) restricted diffusion with $D = (2.3 \pm 1.9) \times 10^{-9} \text{ cm}^2/\text{s}$ at the exterior surface of chorionic layers; (ii) partially restricted diffusion with $D = (3.3 \pm 2.4) \times 10^{-9} \text{ cm}^2/\text{s}$ at the interface of chorionic space and inner mass of embryo; and (iii) random Brownian motion with $D = (4.9 \pm 0.8) \times 10^{-9} \text{ cm}^2/\text{s}$ in chorionic space, respectively.

(b) from representative (i) orange and (ii) green Au nanoparticles in egg water. Both nanoparticles display random Brownian motion with $D = (1.4 \pm 1.0) \times 10^{-8} \text{ cm}^2/\text{s}$ and $(2.7 \pm 2.5) \times 10^{-8}$, respectively.

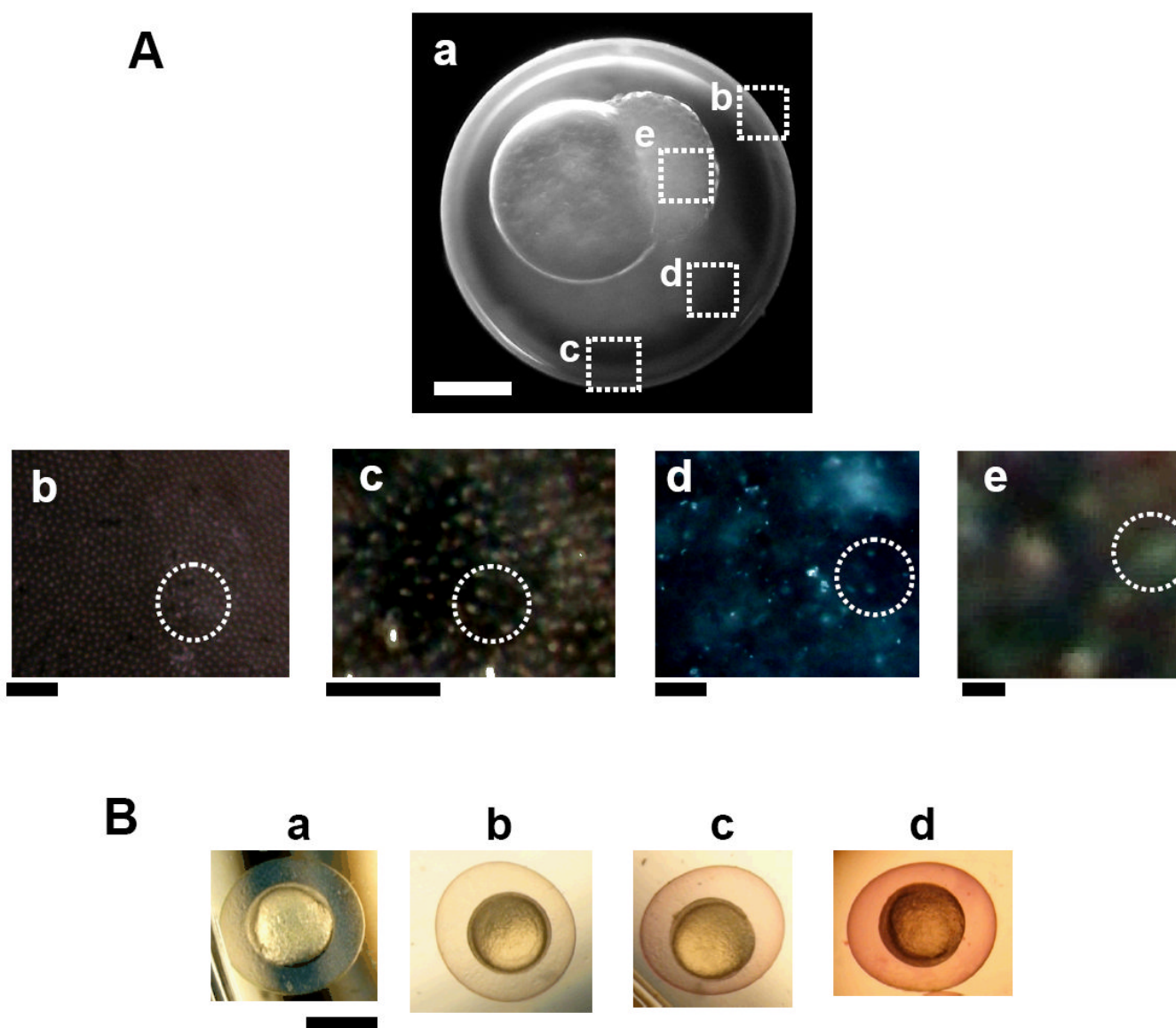


Figure 5. Characterization of Au nanoparticles in zebrafish embryos using dark-field microscopy and spectroscopy.

(A) Representative optical image of (a) a cleavage-stage embryo shows single Au nanoparticles with multiple colors in (b) the top and (c) bottom of the chorionic surface, illustrating well-organized chorionic pores; (d) in chorionic space and (e) in inner mass of the embryo, as squared in (a). The tissue offers a dark-background, while embedded single Au nanoparticles give off LSPR spectra (colors). A few representative nanoparticles embedded in the tissues of interest are circled in (b-e) to help the identification of nanoparticles. We do not highlight all embedded Au nanoparticles, in order to enhance the clarity of the presentation. Scale bar = 200 μm in (a), 20 μm in (b-c), 100 μm in (d), and 1 μm in (e), which shows the distance among individual nanoparticles, but not the sizes of nanoparticles, due to optical diffraction limit of optical imaging. The enlarged images of (be) are included in the Supporting Information.

(B) Optical images of the gastrulation-stage embryos in (a) egg water alone and incubated with (b) 0.05, (c) 0.20, and (d) 1.20 nM Au nanoparticles for 4 h since its cleavage stage. The embryos in (b-d) show the reddish and darken burgundy color of Au nanoparticles, suggesting that the amount of accumulated Au nanoparticles in the embryos increases with concentration. Scale bar = 500 μm . Note that the cleavage-stage embryos develop to gastrulation stage in 4 h. Color images in (A: b-c) and (B) are acquired by DFOMS equipped with a color digital camera, while an image in (A: a) is acquired by CCD camera.

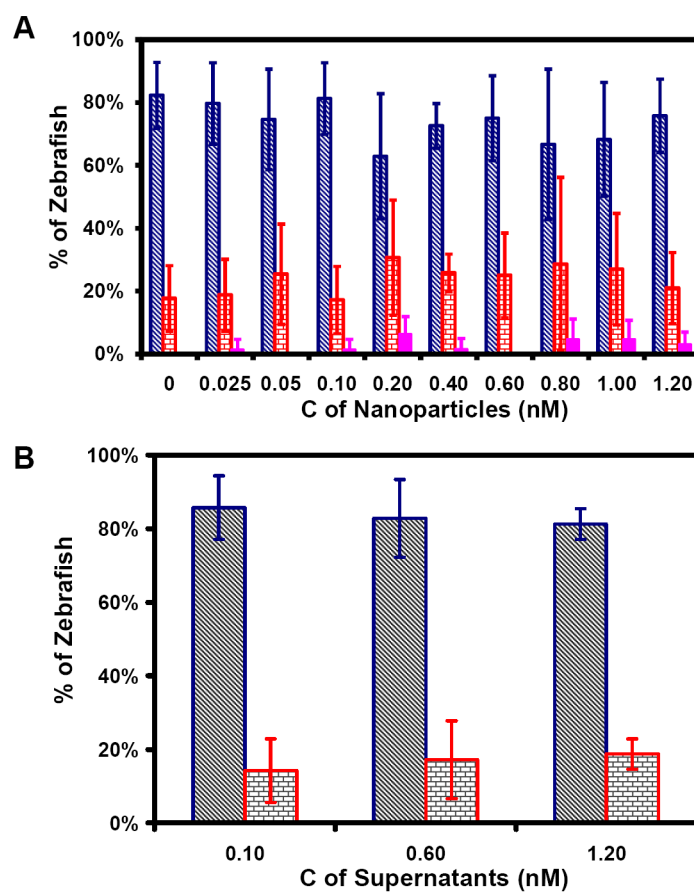
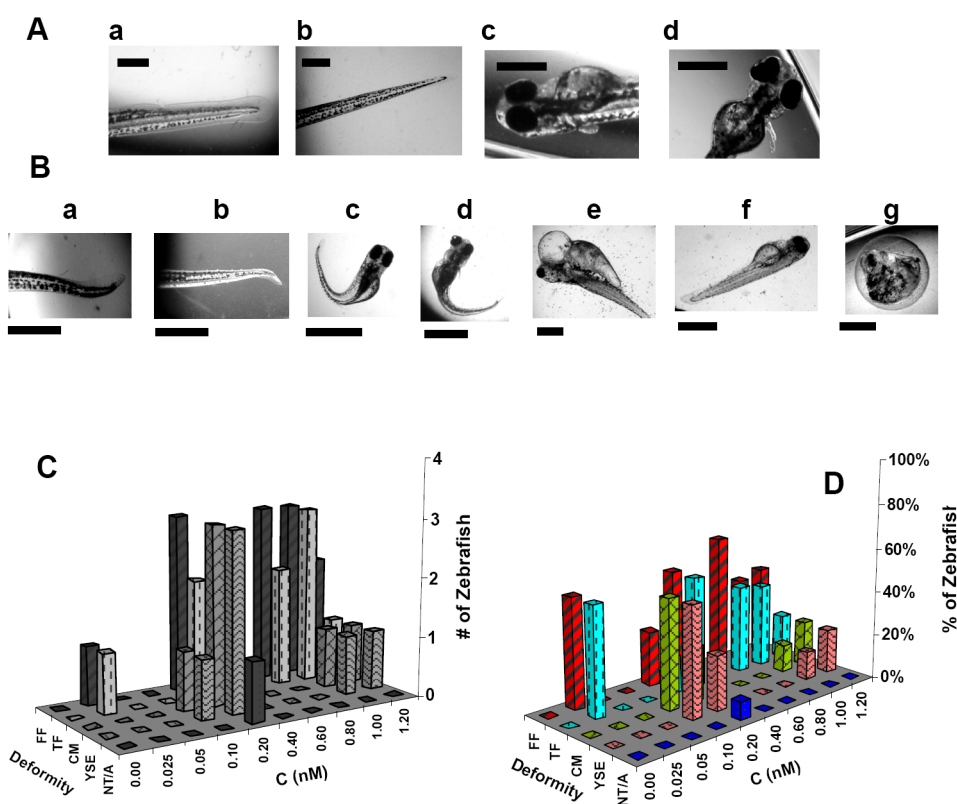


Figure 6. Effects of Au nanoparticles on embryonic development:
(A) Histogram of distribution of normally developed (blue), dead (red), and deformed (pink) zebrafish versus concentration of Au nanoparticles;
(B) Histogram of distribution of normally developed (blue) and dead (red) *versus* concentration of supernatant removed from washing Au nanoparticles (negative control).

**Figure 7.**

Normal and deformed Zebrafish resulted from being treated chronically with Au nanoparticles since their cleavage stage.

(A) Representative optical images of normally developed zebrafish show the normal development of (a) finfold; (b) tail/spinal cord; (c) cardiac and yolk sac; and (d) head and eyes. Scale bar = 500 μ m.

(B) Representative optical images of zebrafish at a given concentration of Au nanoparticles show several deformities such as (a-b) finfold abnormality; (c-d) tail/spinal cord flexure and truncation; (e-f) cardiac malformation and yolk sac edema; and (g) acephaly and no tail. Scale bar = 250 μ m (a, b), 1000 μ m (c-f), and 500 μ m (g).

(C) Histograms of number of deformed Zebrafish with each type of deformities versus concentration of Au nanoparticles, showing the number of deformed zebrafish with a given type of deformities observed at a given concentration of nanoparticles.

(D) Histograms of the percentages of deformed Zebrafish with each type of deformities versus concentration of Au nanoparticles. The percentages of deformed zebrafish with each type of deformities were calculated by dividing the number of one given type of deformed zebrafish with the total number of all five types of deformed zebrafish observed at a given concentration of nanoparticles, aiming to show possible dependence of types of deformation on nanoparticle concentration. Abbreviations of deformities in (C) and (D) are described as follows: finfold (FF) abnormality in red, tail/spinal cord flexure and truncation (TF) in cyan, cardiac malformation (CM) in green, yolk sac edema (YSE) in pink, no tail and acephaly (NT/A) in blue.

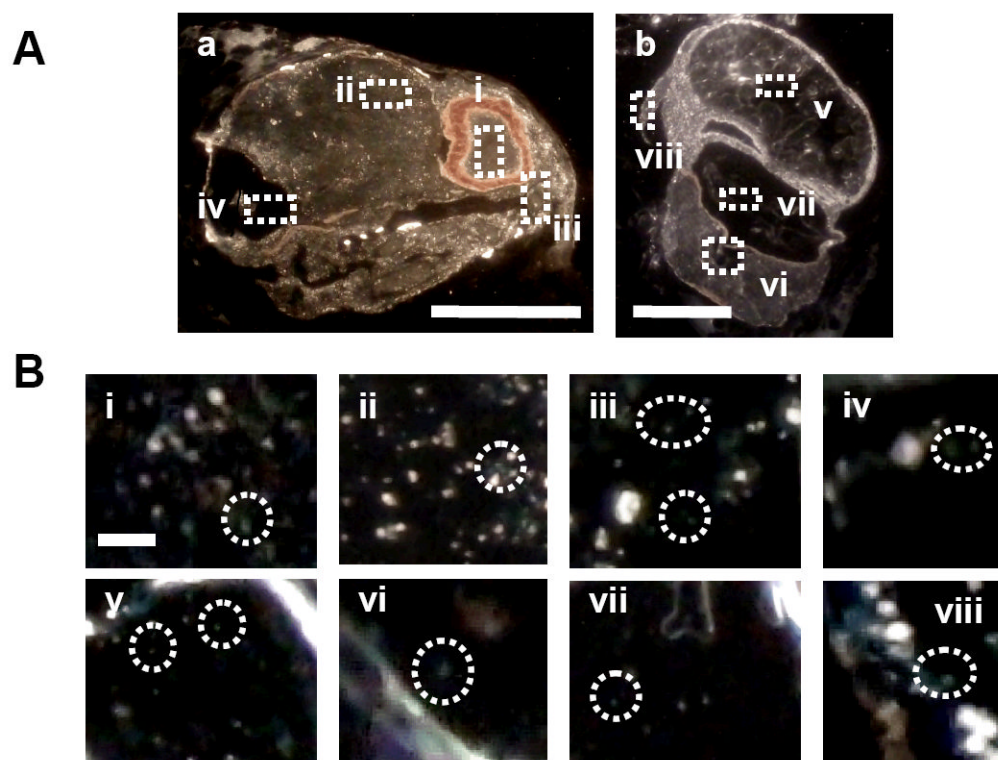


Figure 8.

Characterization of Au nanoparticles embedded in a fully developed zebrafish.

(A) Optical color images of a fixed (a) longitudinal section and (b) cross section of a normally developed zebrafish. The rectangles highlight representative areas: (i) retina, (ii) brain tissue, (iii) nasal sensory epithelium, (iv) otic capsule, (v) stomach, (vi) notochord, (vii) swim bladder, and (viii) pectoral fin. Thickness of tissue sections = $3.5 \pm 0.5 \mu\text{m}$

(B) Zoom-in optical images of those tissue sections outlined in (A). Circles highlight representative individual Au nanoparticles embedded in the tissue sections. Scale bar = $200 \mu\text{m}$ in (A) and $4 \mu\text{m}$ in (B). LSPR spectra of individual embedded nanoparticles are similar to those observed in Figure 2C, showing that they are indeed Au nanoparticles and majority of embedded nanoparticles remain non-aggregated.